A NEW METHOD FOR SEPARATING SURFACE GRAVITY WAVES FROM ADCP MEASUREMENTS

By

CHLOÉ DAISY WINANT

A DISSERTATION PRESENTED TO THE GRADUATE SCHOOL
OF THE UNIVERSITY OF FLORIDA IN PARTIAL FULFILLMENT
OF THE REQUIREMENTS FOR THE DEGREE OF
DOCTOR OF PHILOSOPHY

UNIVERSITY OF FLORIDA

2011

To Papa et Maman

ACKNOWLEDGMENTS

Thanks go to my Graduate advisor, Arnoldo Valle-Levinson, for his generosity and support. His enthusiasm for teaching and learning are an inspiration for everyone with whom he works, and his commitment to the graduate students he mentors is paramount. I thank my PhD committee, Dr Bob Dean, Dr Tom Hsu, Dr Jon Martin, and Dr Bob Thieke, for their patient feedback and guidance. I sincerely appreciate their involvement in this work. I am grateful to Aurelien Ponte for leading the way on many aspects of this research, most importantly with the computational analysis. I owe thanks to Bob Beardsley for his brilliant idea, and to Alex Souza and Bob Guza for their enthusiastic feedback.

For providing a rigorous and fun place to learn, I thank the faculty and staff in the University of Florida Civil & Coastal Engineering Department. I wish to acknowledge funding for this work, notably from the National Science Foundation. Additional financial support was provided by the University of Florida Graduate Alumni Fellowship Program.

I am thankful for my father, my biggest supporter, who pushed me to pursue interesting research and to be technically sound in doing so. I am especially grateful to my mother and my sister, for their loving encouragement and humor and to Liz for her insights. Thanks go to my friends in Gainesville for being there for me whenever I needed them, especially: Amy, Jill, and Sara. Finally, for being my rock, I thank Milan.

TABLE OF CONTENTS

LIST OF TABLES

LIST OF FIGURES

LIST OF ABBREVIATIONS

ADCP	Acoustic Doppler current profiler
CEOF	Complex empirical orthogonal function
EOF	Empirical orthogonal function
HAF	Horizontal adaptive filtering
VAF	Vertical adapative filtering
VFT	Variance fit technique

Abstract of Dissertation Presented to the Graduate School
of the University of Florida in Partial Fulfillment of the
Requirements for the Degree of Doctor of Philosophy

A NEW METHOD FOR SEPARATING SURFACE GRAVITY WAVES FROM ADCP MEASUREMENTS

By

Chloé Daisy Winant

December 2011

Chair: Arnoldo Valle Levinson
Major: Coastal and Oceanographic Engineering

Currents due to surface-gravity waves, i.e. wind waves, vary over horizontal lengths comparable to the wavelength. When observed by bottom-mounted Acoustic Doppler Current Profilers (ADCPs), the velocities are not necessarily the same at the location of each beam, if the horizontal distance between beams is comparable to the wavelength. In this case the usual assumption (invariant velocities over the beam separation) leads to erroneous estimations of velocity. Here, a method is described that resolves the wind-driven wave field directly from beam velocities, using complex empirical orthogonal functions (CEOF). Results from this method show that a few CEOFs account for a large fraction of the high frequency beam velocity variance. The vertical structure of the CEOF mode agrees with wave theory: the frequency of the time dependence of the mode (determined by spectral methods) and the wavenumber (determined by the vertical structure of the mode) are consistent with the dispersion relation for linear intermediate water waves. Once the wave signal is identified, Reynolds stresses corresponding to waves are calculated and compared to wind-stresses. It is shown that the wave Reynolds stresses can be larger than the wind stresses. These wave stresses are proposed to generate a circulation structure that

differs from that predicted by theoretical results of wind-driven flow. Therefore, it is postulated here that wave stresses should be an important contributor to circulation in wind-driven embayments as supported by observations.

CHAPTER 1
HILBERT EOF METHOD

Introduction

Wind-driven waves are influential to the circulation in bays, estuaries and lagoons, by producing both fluctuating and steady currents. Separating current fluctuations caused by waves and turbulence has received considerable attention recently (Trowbridge 1998, Whipple et al. 2006, Rosman et al. 2008, Kirincich et al. 2010). The task is complicated by the horizontal scale of variation associated with short period motions (<10s), which can be comparable in scale with the measuring volume that characterizes an observation. In the case of concern here, the wavelength of an intermediate depth surface gravity wave (typically 20-70m) may be comparable to or smaller than the beam separation (typically 5-20m) of an Acoustic Doppler Current Profiler (ADCP). This study has two objectives. First, to propose a method, based on analysis of separate ADCP beam velocities, which identifies the velocity induced by waves. Second, to determine shear stresses caused by waves and compare them to wind stresses. It is shown that the waves have associated stresses that are larger than the wind stress.

Background

While the circulation in bays and estuaries is often described in terms of components driven by winds, tides, and buoyancy forcing, surface gravity waves are commonly observed, sometimes reaching large amplitudes and breaking. This process is inherently non-linear (Stokes 1847). Non-linear surface gravity waves can drive steady circulation patterns, a rich subject in the field of Surfzone and Nearshore Dynamics (Bowen 1969, Longuet-Higgins 1970, Fedderson et al. 1998), but one that is

rarely considered in studies of the circulation in bays and estuaries. In part, this is because surface gravity waves are difficult to measure, either with bottom mounted pressure sensors or with ADCPs processed using the conventional methods. It can happen that the surface waves are short enough that their signature on the bottom is small, and so they are difficult to detect with a bottom pressure sensor. While ADCPs make measurements of beam velocity to within a few meters from the surface, their interpretation is problematic when the distance between opposite beams (from now on called beam separation) is comparable to the wavelength in distance. An example of this is given in the first paragraph of the Analysis section. Moreover, determination of turbulence properties in areas of the water-column influenced by waves is challenging because of the fluctuating velocities associated with waves.

In observational studies of turbulence based on ADCP observations, it is recognized that the near surface beam velocities include components associated with surface gravity waves. Several methods have been suggested in the past to remove wave bias from beam velocities, and therefore produce estimates of Reynolds stresses[1] induced by turbulence. These include the Variance Fit method proposed by Trowbridge (1998) and later extended to ADCPs by Whipple et al. (2006), and the Vertical and the Horizontal Adaptive Filtering methods (Rosman et al. 2008). The Variance Fit technique is severely limited by the assumption that the wave phase is constant along a beam, as noted in Rosman et al. (2008). Rosman et al. (2008) suggest two methods as alternatives to the Variance Fit method. The first, Vertical Adaptive Filtering, suggested

[1] Here the term Reynolds stress is used as defined by the variance method and represented in Equation 1-1, consistent with Lohrmann et al. (1990), Trowbridge (1998) and Rosman et al. (2008), whether the stress is due to turbulence, waves or any other process.

by Shaw and Trowbridge (2001) relaxes several assumptions that characterize the Variance Fit technique, notably the assumption of constant phase along the beam. The second method, Horizontal Adaptive filtering, considers measurements at the same depth but along different beams. The further refinement afforded by Horizontal Adaptive filtering removes ambiguities associated with the possibility that turbulent eddies can coherently affect different bins on the same beam. The technique presented in this research overcomes the same limitation by specifically evaluating the phase of the velocities along each beam. It is applied to observations at a wind-driven bay in the Gulf of California, Mexico.

Observations

Bahía Concepción

Bahía Concepción, located on the eastern shore of the Baja California peninsula, (Figure 1-1), was the site of a year-long observational program to document the wind-forced circulation in a deep bay. The elongated bay, 40 km long by 5 to 10 km wide, is the result of land down-throw near a geological fault zone (McFall 1968, Johnson and Ledesma-Vásquez 2001). The Bay is separated from the Sea of Cortez, also known as the Gulf of California or Vermillion Sea (for its red tides), by a 15 m deep sill. Immediately south of the sill, a U-shaped channel progressively widens and deepens into the main basin, where the depth is close to 30 m, except near the steep sides. A gently sloping beach closes the Bay in the South. During the winter and spring the Bay is subjected to “Nortes", strong winds (>0.1 Pa) that blow toward the southeast, along the axis of the adjacent sea. In the area of interest, these winds have a strong diurnal modulation, reaching maximum speed in the afternoon, corresponding to a maximum wind stress near 0.1 Pa, as illustrated in the top left panel of Figure 1-2. Inside the bay,

these windy periods correspond to the time when short (periods near three seconds, see also Caliskan and Valle-Levinson 2008) surface gravity waves are observed to grow to large amplitude (1-1.5m), with breaking observed throughout the Bay in the late afternoon.

Because of its location near the semi-diurnal amphidrome described by Morales and Gutiérrez (1989), and Hendershott (1971), the tide in Bahía Concepción is mixed with diurnal dominance, as illustrated in the top right panel of Figure 1-2. The amplitude is of order 0.5 m.

Overview of Measurements

Four Teledyne RD Instruments ADCPs (1200kHz and 600kHz) were deployed on a transect across the Bay, as illustrated in Figure 1-1. Details of the instrument deployments are summarized in Table 1-1 and also described in Cheng et al. (2010).

The instruments were set to record one second ensembles of beam velocities (Mode 12) with the objective of describing the high frequency components of the circulation. Velocity data were rotated to principal-axis and cross-axis components obtained by linear regressions. The coordinate system used here has the x-axis running in the along-bay direction, parallel to 130 deg, and the y-axis points 40deg. Reynolds stresses were estimated from the top bins of each ADCP, over a ten minute interval. At each bin, for each ADCP, the Reynolds stress is estimated following the variance method (Lohrmann et al. 1990, Trowbridge 1998, Lu and Lueck 1999b, Whipple et al. 2006, Rosman et al. 2008). Here, the two components of stress are estimated as:

$$R_{21} = \rho \overline{\frac{b_{2t}^2 - b_{1t}^2}{2\sin 2\theta}} \qquad R_{43} = \rho \overline{\frac{b_{4t}^2 - b_{3t}^2}{2\sin 2\theta}} \tag{1-1}$$

where $\overline{b_{\mathrm{nt}}^2}$ is the variance over ten minutes of the beam velocity for beam n, $(n = 1, 2, 3, 4)$, and the top bin, and ρ is the water density.

These stresses, rotated along principal axes and calculated from the raw data, are illustrated in the lower left-hand panels of Figures 1-2. They are characterized by large peaks that are synchronous with the wind events. Remarkably, in three of the four cases, the Reynolds stresses are of order 1 Pa, which exceed the wind stresses by one order of magnitude. The stresses decay to near zero over the top 10 meters of the water column. The cause of these large Reynolds stresses is the central issue explored in this paper.

Fluctuations in the vertically averaged horizontal velocity at each site are illustrated in the lower right-hand panels of Figures 1-2. The largest fluctuations appear to be related to the tidal variation as indicated by pressure. Winds seem to play a secondary role in the depth-averaged variables.

To explore the provenance of the large stresses illustrated in Figures 1-2, spectral density estimates of the variance in the top bin of beam 1 are illustrated in Figure 1-3 for each ADCP. Beneath the wave frequencies (frequency <0.1 Hz), variance increases with decreasing frequency. In the wave band, each spectrum has a significant peak centered at about 0.3 Hz, corresponding to a period near three seconds and related to seas. The variance in this band decreases from the west side of the Bay to the sheltered east side.

Spectra from all depth bins at the west site are illustrated in Figure 1-4. The spectra are ordered so that the top line corresponds to the bin closest to the surface, and the line closest to the abscissa corresponds to the bin closest to the bottom, as

would be expected for a deep water wave. These results suggest that the large stresses described in Figure 1-2 may be associated with surface gravity waves and indicate that the maximum wave energy is close to the surface and decreases with depth. A method to separate the wave signal from the measurements is described next.

Analysis: The Hilbert EOF method

An acoustic Doppler current profiler (ADCP) measures velocity along the axis of each of its four transducer beams, as a function of time and distance from the acoustic transducer. In many cases, when the actual velocities change little over the horizontal surface intersecting the four beams, velocities in the earth reference frame can be directly estimated with a coordinate transformation provided by the manufacturer. When the velocity changes over distances comparable to the beam separation, this method is no longer useful, as in the case of deep water waves. For example, a three second wave in a water depth of 16.5 m has a wavelength of 20 m, while the distance between opposite beams, near the surface, is about 10 m. In this case there is no simple transformation between beam velocities and earth coordinates. Instead, attention is focused on the amplitude and phase of the observed beam velocities, and how these compare to what surface gravity wave theory predicts for beam velocities.

Because of the narrow band nature of the high-frequency spectral peaks (illustrated in Figures 1-3 and 1-4), the beam velocities are first high-pass filtered to remove fluctuations with periods longer than thirty seconds. This should isolate the wave signal. Then in order to preserve the phase information, each beam velocity is replaced by its Hilbert transform (Emery and Thomson 2001): the real part of the complex time series is the original observation and the imaginary part is phase shifted by $\pi/2$. Principal modes of co-variation are then determined by finding the eigenvalues

and eigenfunctions of the complex co-variance matrix (Emery and Thomson 2001). This is the Hilbert Empirical Orthogonal Functions (EOF) or Complex EOF (CEOF).

To understand how the Hilbert EOF method works, it is helpful to consider, for instance, a time series of temperature observations at multiple sites around the world. If the major signal at each station consists of a diurnal variation reaching maximum temperature in the afternoon, local time, and if all the observations are entered in universal time, they will have a variable phase. An EOF analysis of these signals will return two modes, uncorrelated at zero lag, but highly correlated at a six hour lag. If, instead, the procedure described above is applied, and the EOF analysis is carried out using the covariance of the Hilbert transformed data, a single mode will account for most of the variability, and the amplitude and phase will be determined for each station. Thus it is anticipated that if a single wave is responsible for the stresses illustrated in Figure 1-2, the amplitude and phase of the largest mode based on an analysis of all the beam velocities at all depths for a single instrument should behave in a manner consistent with linear wave theory.

Linear Theory

The along-beam velocities measured by a four beam ADCP can be predicted from linear theory as follows. Consider an intermediate water wave progressing toward +y, (to stay consistent with Rosman et al. 2008), over a 4 beam ADCP. The plane defined by beams 3-4 makes an angle α with the y-axis, as illustrated in Figure 1-5.

If the sea level perturbation due to the wave is expressed as:

$$\eta(x, y, t) = A\cos(\boldsymbol{k} \cdot \boldsymbol{x} - \sigma t) \tag{1-2}$$

where A represents the amplitude of the wave, σ is the frequency, $\boldsymbol{x}$ is the horizontal position vector and $\boldsymbol{k}$ is the two-dimensional wavenumber vector, the magnitude of which is related to the frequency by the dispersion relation:

$$\sigma^2 = g|\boldsymbol{k}| \tanh(|\boldsymbol{k}|h) \tag{1-3}$$

then, following for example Dean and Dalrymple (1991), the horizontal and vertical velocities are:

$$u(x,y,z,t) = \frac{\sigma A}{\sinh|\boldsymbol{k}|h}[\cosh|\boldsymbol{k}|(z+h)\cos\alpha\cos(\boldsymbol{k}\cdot\boldsymbol{x}-\sigma t)] \tag{1-4}$$

$$v(x,y,z,t) = \frac{\sigma A}{\sinh|\boldsymbol{k}|h}[\cosh|\boldsymbol{k}|(z+h)\sin\alpha\cos(\boldsymbol{k}\cdot\boldsymbol{x}-\sigma t)] \tag{1-5}$$

$$w(x,y,z,t) = \frac{\sigma A}{\sinh|\boldsymbol{k}|h}[\sinh|\boldsymbol{k}|(z+h)\cos(\boldsymbol{k}\cdot\boldsymbol{x}-\sigma t)] \tag{1-6}$$

The along beam velocity (defined positive toward the transducers) for each beam can be written as:

$$b_{n1} = \frac{\sigma A}{\sinh|\boldsymbol{k}|h}[\cosh|\boldsymbol{k}|(z_n+h)\sin\theta\sin\alpha\cos(\boldsymbol{k}\cdot\boldsymbol{x_{n1}}-\sigma t) - \sinh|\boldsymbol{k}|(z_n+h)\cos\theta\sin(\boldsymbol{k}\cdot\boldsymbol{x_{n1}}-\sigma t)] \tag{1-7}$$

$$b_{n2} = \frac{-\sigma A}{\sinh|\boldsymbol{k}|h}[\cosh|\boldsymbol{k}|(z_n+h)\sin\theta\sin\alpha\cos(\boldsymbol{k}\cdot\boldsymbol{x_{n2}}-\sigma t) + \sinh|\boldsymbol{k}|(z_n+h)\cos\theta\sin(\boldsymbol{k}\cdot\boldsymbol{x_{n2}}-\sigma t)] \tag{1-8}$$

$$b_{n3} = \frac{-\sigma A}{\sinh|\boldsymbol{k}|h}[\cosh|\boldsymbol{k}|(z_n+h)\sin\theta\sin\alpha\cos(\boldsymbol{k}\cdot\boldsymbol{x_{n3}}-\sigma t) + \sinh|\boldsymbol{k}|(z_n+h)\cos\theta\sin(\boldsymbol{k}\cdot\boldsymbol{x_{n3}}-\sigma t)] \tag{1-9}$$

$$b_{n4} = \frac{\sigma A}{\sinh|\boldsymbol{k}|h}[\cosh|\boldsymbol{k}|(z_n+h)\sin\theta\sin\alpha\cos(\boldsymbol{k}\cdot\boldsymbol{x_{n4}}-\sigma t) - \sinh|\boldsymbol{k}|(z_n+h)\cos\theta\sin(\boldsymbol{k}\cdot\boldsymbol{x_{n4}}-\sigma t)] \tag{1-10}$$

where θ is the angle formed by the beam and the vertical. Each beam velocity is the vector sum of two parts, the first is the contribution from the horizontal velocity, and the second is the contribution due to the vertical velocity. If l represents the distance from the bottom to the center of the first bin and Δl represents the bin separation, then the location beneath the surface of each bin z_n is given by $z_n = (l + (n-1)\Delta l))\cos\theta - h$. The horizontal position of each bin on beam 1, for instance, is given by $|\boldsymbol{x}_{n1}| = -(l +$

$(n-1)\Delta l))\sin\theta\sin\alpha$, and the horizontal position for beam 3 is $|\boldsymbol{x}_{n3}| = (l + (n - 1)\Delta l))\sin\theta\cos\alpha$, as illustrated in Figure 1-5.

The beam velocities can also be expressed as amplitude and phase. If Equations 1-7 through 1-10 are written as:

$$b_{nb} = H_{nb}\cos(\boldsymbol{k}\cdot\boldsymbol{x_{nb}} - \sigma t) + V_{nb}\sin(\boldsymbol{k}\cdot\boldsymbol{x_{nb}} - \sigma t) = A_{nb}\cos(\boldsymbol{\varphi_{nb}} - \sigma t) \tag{1-11}$$

the amplitude and phase are related to vertical and horizontal components by:

$$A_{nb} = \sqrt{H_{nb}^2 + V_{nb}^2} \qquad \varphi_{nb} = \boldsymbol{k}\cdot\boldsymbol{x_{nb}} - \tan^{-1}\left(\frac{V_{nb}}{H_{nb}}\right) \tag{1-12}$$

Before attempting to compare with observations, some estimates of the wave parameters (frequency, orientation of the wave, mean amplitude) are required.

Determining Wavenumber

The wavenumber $\boldsymbol{k}h$ of the observed wave is determined using two values of vertical velocity w along a single beam at the height z_{nb} and the height two bins below, z_{nb-2}. The ratio of the amplitudes can be expressed using linear wave theory (Equation 1-6) as:

$$w(x,y,z_{nb},t)\Big/w(x,y,z_{nb-2},t) = \sinh|\boldsymbol{k}|(z_{nb}+h)\Big/\sinh|\boldsymbol{k}|(z_{nb-2}+h) \tag{1-13}$$

Define $z_{nb} = (z_{nb}+h)/h$ for the top bin of an ADCP, and $z_{nb-2} = (z_{nb-2}+h)/h$ is the corresponding value for two bins beneath the top bin, the ratio is then:

$$w(x,y,z_{nb},t)\Big/w(x,y,z_{nb-2},t) = \sinh(z_{nb} * \boldsymbol{k}h)\Big/\sinh(z_{nb-2} * \boldsymbol{k}h) \tag{1-14}$$

Thus it is possible to find $\boldsymbol{k}h$ numerically such that the right hand side is equal to the left.

Following the steps defined above, in the case of ADCP West, the depth of the ADCP h, is 16.5 m below the surface and there are 11 good bins. Bin 11 is 4 m beneath the surface, thus $z_{n11} = \frac{12.5}{16.5} = 0.7515$, while $z_{n9} = \frac{10.5}{16.5} = 0.64$. If the ratio of the velocity amplitudes is found to be $\frac{w(z_{n11})}{w(z_{n9})} = 1.9$ for example, then $\boldsymbol{k}h$ would be the solution to the transcendental equation:

$$1.9 = \sinh(0.7515 * \boldsymbol{k}h) \Big/ \sinh(0.64 * \boldsymbol{k}h) \tag{1-15}$$

The solution, found numerically by using Newton's method is:

$$\boldsymbol{k}h = 5.75 \tag{1-16}$$

If $\boldsymbol{k}h$ is large (>3) the wavenumber can be estimated directly:

$$1.9 = \exp(0.1115 * \boldsymbol{k}h) \quad or \quad \boldsymbol{k}h = \ln(1.9)/0.1115 = 5.75 \tag{1-17}$$

Knowing $\boldsymbol{k}h$, the dispersion relation gives $(\sigma^*)^2 = g^* \boldsymbol{k}h \tanh \boldsymbol{k}h \,/h$, where σ^* is in rad/sec. In the example above for $\boldsymbol{k}h = 5.75$, σ^* is computed to be 0.28 Hz. Then σ^* can be compared to the peak frequency, as determined by the spectra, σ_s^*. In Figure 1-4, the frequency at which the peak energy for the surface bin occurs is $\sigma^* = 0.28\, Hz$. The close agreement between σ_s^* and σ^*, determined from the product $\boldsymbol{k}h$ and the dispersion relation, strongly argues that the covarying pattern defined by the largest Hilbert EOF mode corresponds to an intermediate depth surface gravity wave.

Results for the four moorings are summarized in Table 1-2. We see good agreement between the frequencies determined using the two methods described above. Results from Table 1-2 confirm that the circulation captured by the first mode of the Hilbert EOF is very likely caused by surface gravity waves.

Determining the Wave Amplitude

The amplitude of the observed wave,A, is estimated using the eigenvalue of the largest CEOF, λ_1. When computing the synthetic time series, the wave is assumed to have an amplitude of 1 m, so the eigenvalue for the synthetic time series, λ_s, corresponds to $\frac{H}{s} = 1m$. Since the eigenvalues are proportional to variance, A^2, the observed amplitude is represented by $A = \sqrt{\lambda_1/\lambda_s}$.

Determining the Wave Orientation

If the beams happen to be at a right angle to the wave direction (corresponding to $\alpha = 0$), then the beam velocities are only influenced by the vertical velocities. If $\alpha \neq 0$, the same method is used, choosing the beam for which the variance is a minimum because this will be the beam where the vertical velocity has the least influence. However, the answer is only an estimate.

Consider a wave propagating along the y-axis, from beam 4 toward beam 3 as in Figure 1-5. Peaks and troughs will pass beam 3 after beam 4. If the beam velocities are principally the result of vertical velocities (the deep water limit), the difference in phase between beams 3 and 4 would be expected to be positive, and the magnitude of the phase difference would be related to the wave number. The actual beam 3 and beam 4 velocities (Equations 1-9 and 1-10) are a combination of both vertical and horizontal velocities. The phase difference between beams 3 and 4, φ_{34}, is illustrated in Figure 1-6, as a function of the product of the wavenumber by the beam separation, $\boldsymbol{k} \cdot s$. The water depth h is 16.5 m, and the beam separation for the topmost bin is:

$$s = 2 * h\, sin\theta = 2 * (11 + 1)\sin(20) = 8.5\, m \qquad (1\text{-}18)$$

If $\boldsymbol{k} \cdot s$ is very small, the waves are shallow water waves, the wavelength is very long, and the beam velocities are sensitive to only the horizontal component of velocity. Equations for velocities along beam 3 and beam 4 (Equations 1-9 and 1-10) make it clear that the velocities are of equal magnitude and opposite sign, so that $\varphi_{34} = \pi$. As $\boldsymbol{k} \cdot s$ increases, the arguments $\boldsymbol{k} \cdot \boldsymbol{x}_{n3}$ and $\boldsymbol{k} \cdot \boldsymbol{x}_{n4}$ change in such a way that φ_{34} first decreases, even though the beam velocities are still dominated by the horizontal velocities. When $\boldsymbol{k} \cdot s$ increases beyond 0.5, the vertical velocities become important, and φ_{34} increases, until it reaches π. This is when the beam separation is just wide enough that both beam velocities appear to be in phase. If the beam velocities were sensitive to only the vertical or the horizontal velocities, this would occur when $\boldsymbol{k} \cdot s = \pi$ For even larger values of $\boldsymbol{k} \cdot s$, φ_{34} increases anew, with period-wraps that occur at intervals near π, because at these large values of wavenumber, the beam velocities are principally dependent on the vertical velocity.

The vertical dependence of the amplitude of the beam velocities and the difference in phase between the two beams are illustrated in Figure 1-7 for three different wave periods (T=3.6, 5, and 7), propagating in 16.5 m water depth. For each period, the amplitude of the wave increases with distance above the bottom. The rate of increase depends on the period. Changes in amplitude are one way to determine the wavenumber. Figure 1-7 also suggests that the phase difference between the two beams is related to the wavenumber. For instance, for bin 8 the phase differences are 1.6 (solid curve), 1.8 (dashed curve) and 2.8 (dash-dotted curve) respectively. It is also clear that the relation between phase difference and wave period is complicated by two factors. First, when the phase difference becomes large enough, it wraps around,

decreasing by 2π, as between bins 9 and 10 for the T=3.6 sec period example. Second, the relation between wavenumber k and phase difference is opposite near the bottom (where the contribution for the horizontal velocity on the beam velocity is largest) from what it is near the surface.

If wave propagation is not parallel to the beam 3-4 plane ($\alpha \neq 0$), the indicated phase difference σ_{34} should decrease relative to σ_{34} at $\alpha = 0$, while at the same time the phase difference between beams 1 and 2 σ_{12} should increase. To quantify this, a synthetic series of beam velocities has been generated using Equations 1-7 through 1-10, for various values of α and different periods. The co-varying modes of variability were determined for each combination of parameters. This is illustrated in Figure 1-8 where the phase differences φ_{12} and φ_{34} are shown as a function of the incidence angle α. For the longer wave period (T=3), the phase differences vary as the cosine and sine of the incidence angle. As expected, if $\alpha = 0$, the phase difference between beams 1 and 2 is zero, and the phase difference between beams 3 and 4 is a maximum, equal to 2.19. For a longer wave (T=3.6), the relationship wraps around, but the same process is being represented.

Comparing Observations to Theory

To compare this proposed new Hilbert EOF theory with observations, synthetic time series of b_{nb} were evaluated using Equations 1-7 through 1-10 where the amplitude A is assumed to be one, the frequency is taken as the peak frequency in the spectrum of the filtered beam velocities, and the remaining parameters are determined by instrument and deployment characteristics. The synthetic beam velocities are subjected to identical analyses applied to the observations. The vertical structure of the

phase and amplitude of the observed along beam velocity for ADCP West is illustrated in Figure 1-9, along with the predictions from linear theory. The agreement with observations is excellent. The amplitudes and phases of the beam velocities match the theoretical profiles extremely well, and have a complex correlation of 0.9905. This remarkably good agreement indicates that the first mode of the observations does correspond to a surface gravity wave. Once the wave signal is distinguished in the orbital velocities, the wave-associated velocity fluctuation may be used to estimate wave Reynolds stresses.

Wave Reynolds Stress

Reynolds stresses are a measure of the flux of momentum that result from the turbulent or periodic fluctuations in a time dependent flow. The stresses are non-linear, time-averaged components of the (3-dimensional) turbulent oscillations. For example, two components of the velocity that are oscillating slightly in phase will have a non-zero co-variance, and generate corresponding non-zero Reynolds stresses.

From Newton's Second Law we know that a change in momentum results from the sum of forces acting on a system. Typically in the open and coastal oceans, the stresses associated with wind, tidal, and buoyancy forcings are considered the most important for understanding fluxes of momentum. New studies (Xu and Bowen 1994) and observations (Fewings et al. 2008) have shown the importance of wind-wave stresses to the vertical flux of momentum in a water column when the rotation of the earth is included in the analysis. For instance, Xu and Bowen (1994) construct an Eulerian model of the steady flow driven by wave stresses, sometimes called Coriolis-Stokes forcing (Polton and Belcher 2005). In a basin, the progressive waves propagating close to the boundaries can become partially reflected. The fluctuating

wave velocities have stresses associated with them. Near the surface, white-capping and wave breaking also produce stresses, however these processes are difficult to measure directly.

Time series of Reynolds stress estimates for ADCP West and ADCP Center West are illustrated in Figures 1-10 and 1-11. Using the variance method (Equation 1-1), the covariance between beams 1 and 2 and beams 3 and 4 are calculated for every ten minute average. In both figures, the top plot represents six days of stress estimates using the raw beam velocities. Reynolds stress estimates have a diurnal signal, peaking at one Pascal. These stress values are 10 times the strength of expected wind stress. The bottom plots represent stress estimates after subtracting the velocities from the first mode (the time series of the first eigenvalue) of each ADCP using the Hilbert EOF method. The first mode is associated with wave velocities. The residual stresses are much smaller than the raw covariances at both locations. Because the stresses are so greatly reduced, we can say that most of the stresses that come from the raw data can be associated with the first mode's waves. It is unclear whether the remaining stresses correspond to real physical processes, such as other waves, winds, or tides, or are simply instrumental noise, but their magnitude and direction are consistent with wind stresses.

Wave Induced Residual Circulation

It is understood that the fluctuating tide can drive a steady circulation in a basin (Li and O'Donnell 2005) such as Bahía Concepción. But can surface gravity waves, another type of oscillatory motion, also produce a steady circulation? Here, I speculate as to what the wave-driven circulation might look like. The steady flows can be divided up into two components. The first is driven by the Stokes drift, and the second is driven

by the time averaged stresses associated with the waves. In both cases, the fact that the wave amplitude increases significantly from the east side to the west side of the basin will produce gradients in this wave-forcing that are likely to produce a gyre like steady circulation.

Away from the boundaries, near the western shore, the average amplitude of the 3 second waves in Bahía Concepción during the observation period is 0.2m. The average frequency is 2 rad/sec and the velocities near the surface are 0.4 m²/s. The Stokes drift $\overline{u\eta}$ is then estimated to be of order 0.1 m²/s. Alternatively, the Stokes velocity can be estimated using Dean and Dalrymple (1991):

$$\overline{u\eta} = \frac{E}{\rho c} = 0.04\ m^2/s \tag{1-19}$$

Because the waves occupy the top few meters of the water column (order $\frac{2\pi}{k} = 3m$), we can estimate the Stokes velocity as being of order 0.03 m/s.

$$\frac{2\pi}{k} u_{stokes} = \overline{u\eta} \tag{1-20}$$

Because the bay is closed, a large Stokes drift would force measurable downwave Stokes velocities on that side. Along the opposite side where waves amplitudes are much smaller, an opposite current would likely develop as a result of mass conservation.

In Figure 1-2 it is shown that wave induced Reynolds stresses reach maximum amplitudes of order 1 Pa when the waves are largest. Given relatively high frequency, the waves will be affected by bottom friction in depths of only a few meters (<10m). The bottom stress will then act to reduce the wave Reynolds stress. The resulting divergence in the wave Reynolds stress is in many ways similar to the process described by Li and O'Donnell 2005. The stress-divergence is expected to be balanced

in part by a downwave sea level rise that is uniform across the width of the bay, and friction due to the steady residual current. In the case of Bahía Concepción, this would correspond to a mean downwave flow on the western side of the Bay at depths less than 5 m, and a compensating flow in the opposite direction on the eastern side. Mass conservation dictates that these two streams be connected by an alongshore drift from west to east in shallow depths along the south shore. A sketch of these flows is illustrated in Figure 1-12.

In Bahía Concepción, a gyre-like circulation patterns was observed by Ponte et al. (2011). These currents were assumed to be driven by the winds and the tides. But it is equally possible that the gyre is driven by the waves, or at least that the wave-circulation that I've just described is consistent with the observations. To further explore this possibility, theory of the circulation induced by waves in small bays and estuaries needs to be further developed.

Conclusions

A method based on Hilbert EOF analysis has been presented that allows the amplitude of surface gravity waves, their frequency wavenumber and direction of propagation to be estimated from Mode 12 ADCP beam velocities, even when the beam separation is comparable to the wavelength. In Bahía Concepción, this method shows that the wave Reynolds stresses can be considerably larger than the stress induced by the wind over the surface, or the stresses associated with tidal forcing. These wave Reynolds stresses vary both with depth and horizontally, in a pattern that would result in a gyre-like circulation in the bay. In fact such a gyre is observed, but has previously been explained by wind forcing alone. The Hilbert EOF method is strictly correct only for narrow band waves.

Table 1-1. Bahia Concepcion ADCP Locations January-February 2005

Station	Depth (m)	Latitude (˚)	Longitude (˚)	Start Time GMT	Samples	Bins	Size (m)	Roll (˚)	Pitch (˚)	Heading (˚)
1 (West 1421)	16.5	26 38.70	-111 49.927	16 Jan 18:30	1372800	11	1	1.4	-1.83	302
2 (CW 5605)	28.2	26 39.201	-111 49.245	15 Jan 18:30	500000	11	2	-3.21	-0.26	136
3 (Center 5510)	25.0	26 38.864	-111 48.413	16 Jan 20:30	1200000	9	2	-1.8	-5.7	99
4 (East 5457)	16.3	26 40.913	-111 47.223	17 Jan 18:30	1200000	11	1	-0.16	-5.0	219

Table 1-2. Bahia Concepcion wave statistics January-February 2005

Station	$\boldsymbol{k}h$	σ^* Hz	σ_s^* Hz	α deg	A m
1 (West)	5.75	0.28	0.28	135	0.07
2 (CW)	7.45	0.26	0.26	100	0.14
3 (Center)	5.7	0.24	0.29	300	0.10
4 (East)	6.6	0.32	0.38[2]	350	0.03

[2] Poorly defined peak

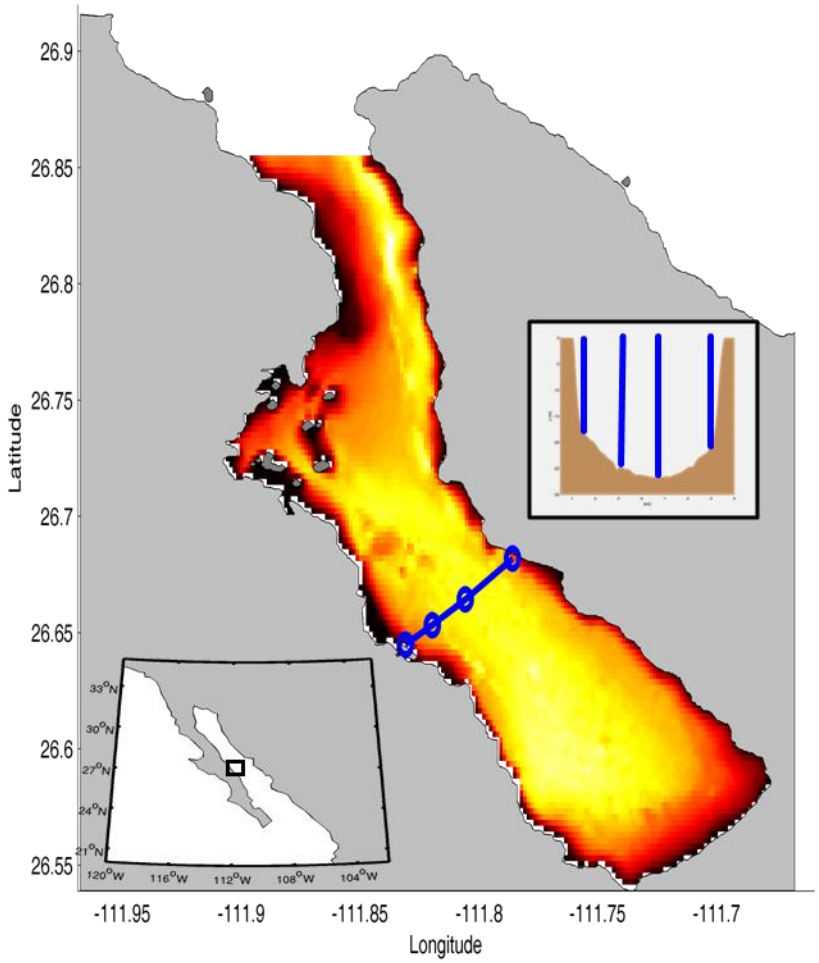

Figure 1-1. Map of Bahía Concepción showing ADCP transect location, with ADCP's West, CW, Center, and East denoted by the blue circles from left to right. Depth is indicated by the color shading with a maximum of 30m. The vertical cross section on the right represents the ADCP line. The position of Bahía Concepción with respect to the Baja Peninsula is represented by the black square on the bottom left map.

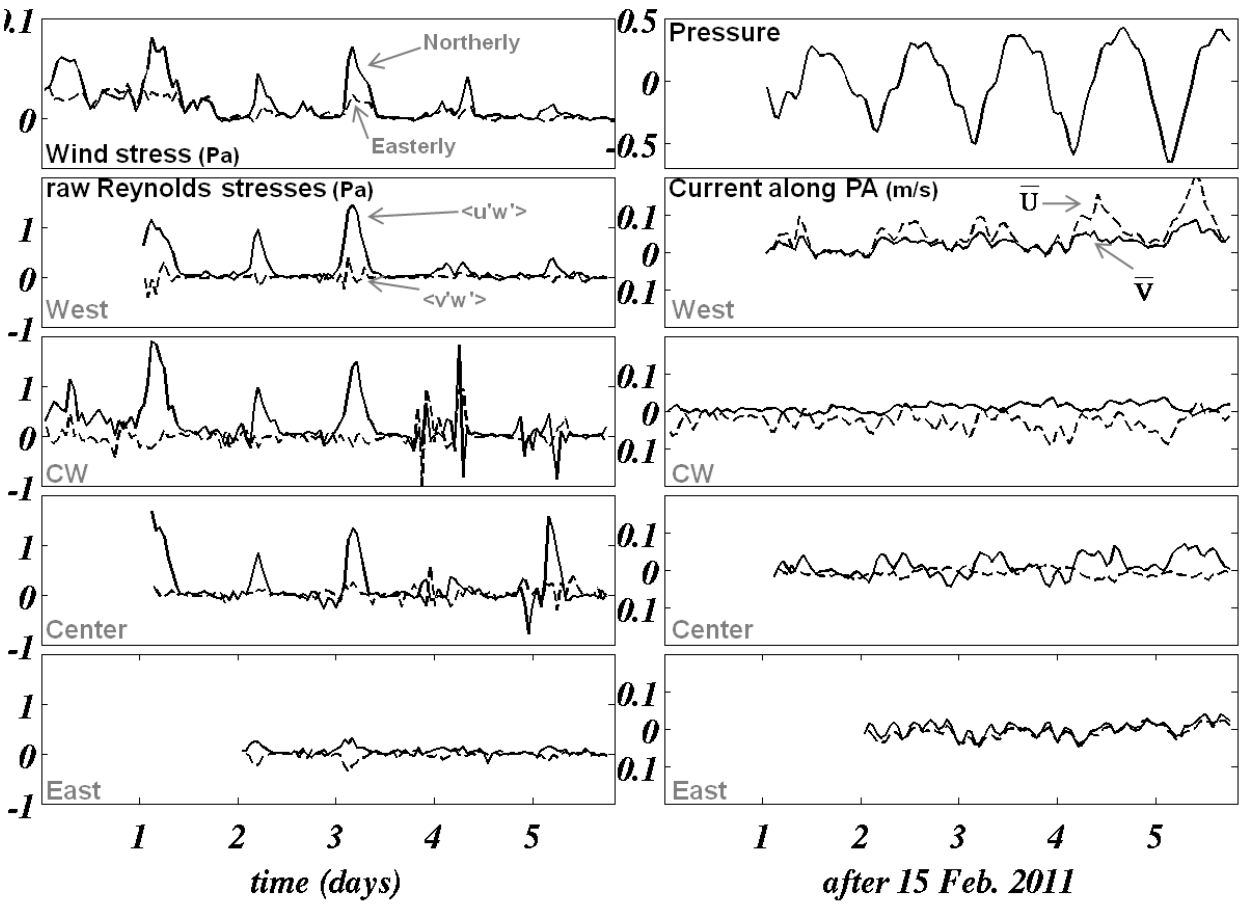

Figure 1-2. Overview of the forcings in Bahía Concepción for the observational period's first five days. Top left: time series of wind stress measured at the North station. Top right: pressure observations in 30 m. Remaining left panels: Reynolds stress estimated from the variance method from ADCP beam variances at the top bin at each ADCP site. Remaining right panels: vertically averaged velocities from each ADCP site

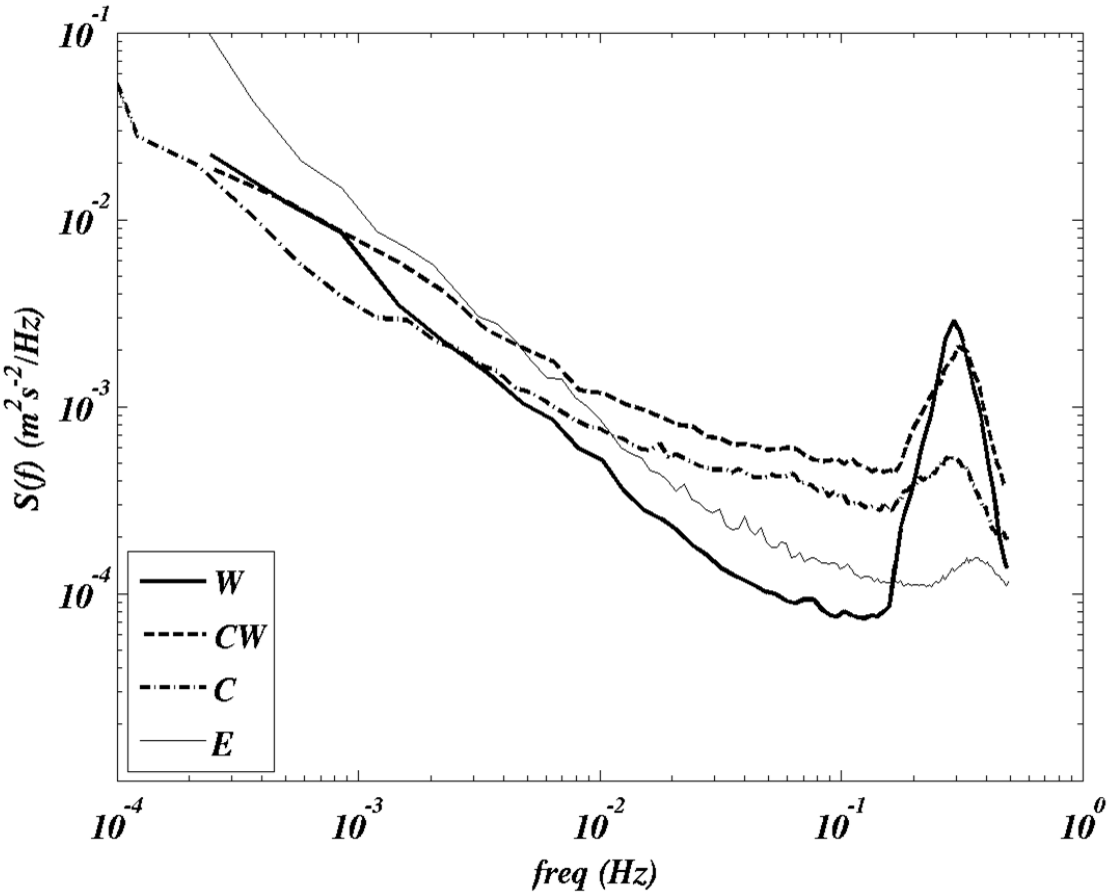

Figure 1-3. Spectra of the top bin beam 1 velocity (all beams are similar) for the four ADCPs.

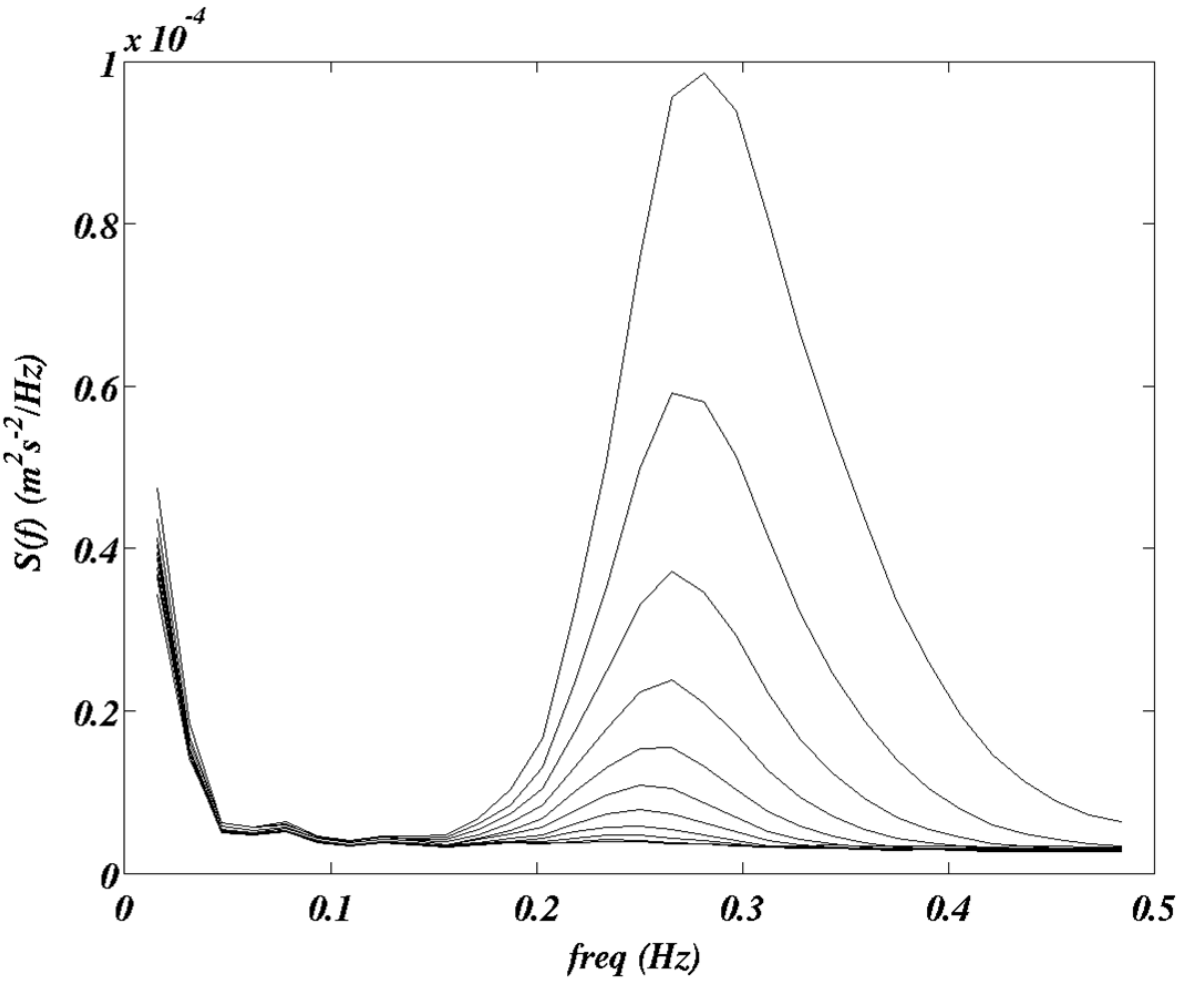

Figure 1-4. Spectra from all bins on beam 1 of the West ADCP. The spectra are ordered so that the top line corresponds to the bin closest to the surface and the line closest to the abscissa corresponds to the bin closest to the bottom.

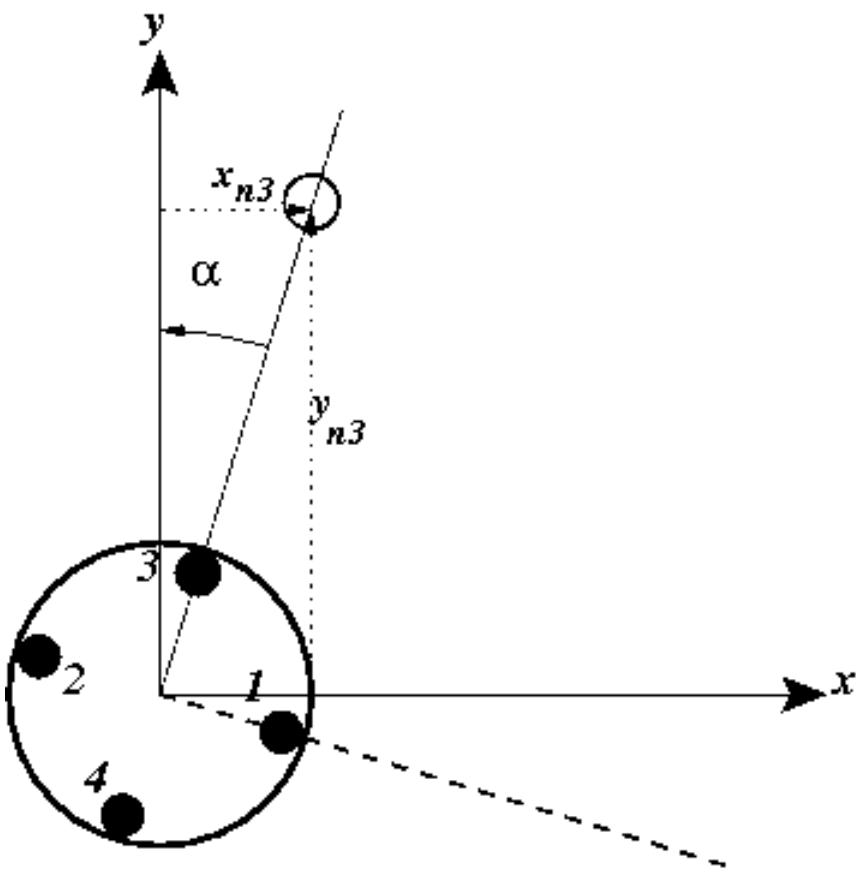

Figure 1-5. Schematic of the ADCP beam geometry. Following Rosman et al. 2008, consider a wave progressing toward +*y*, over an ADCP oriented so that the plane defined by beams 3 and 4 makes an angle α with the y-axis. The open circle denotes the position in the *x*-*y* plane of the nth bin along beam 3

.

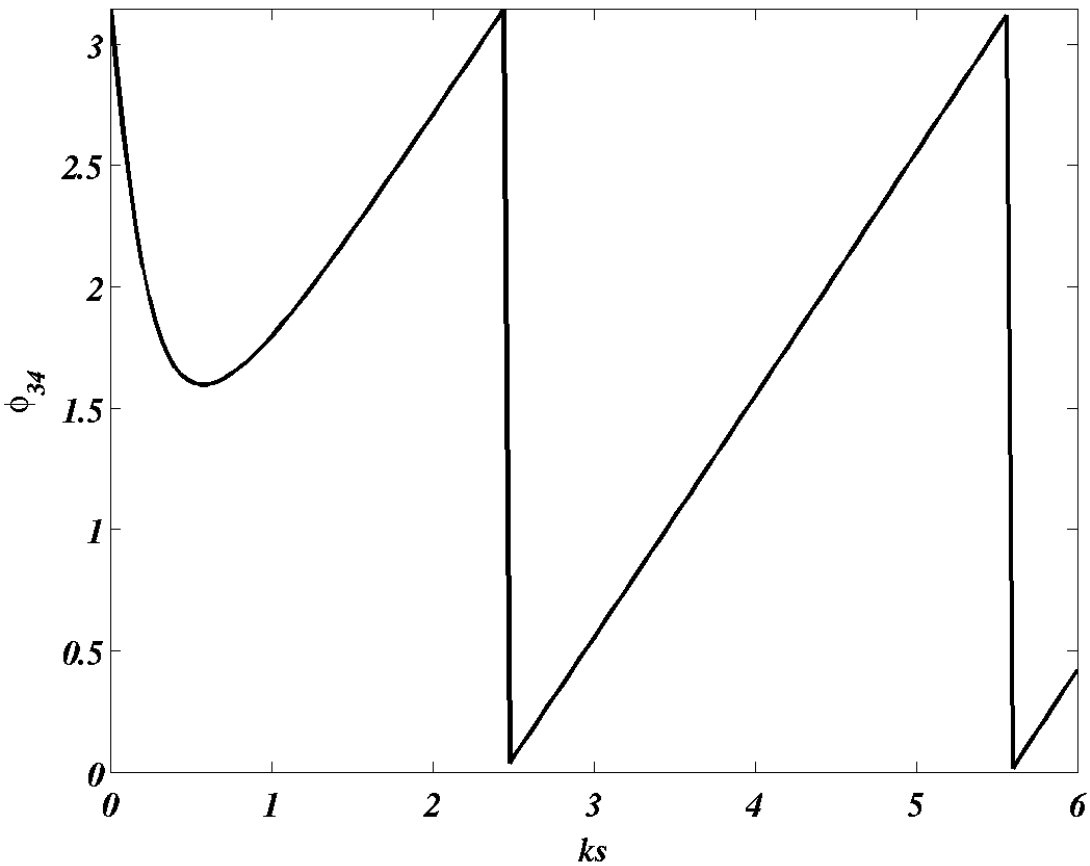

Figure 1-6. Phase difference between beams 3 and 4, for an incidence angle $\alpha = 0$, as a function of the product of the wavenumber by the beam separation $k \cdot s$

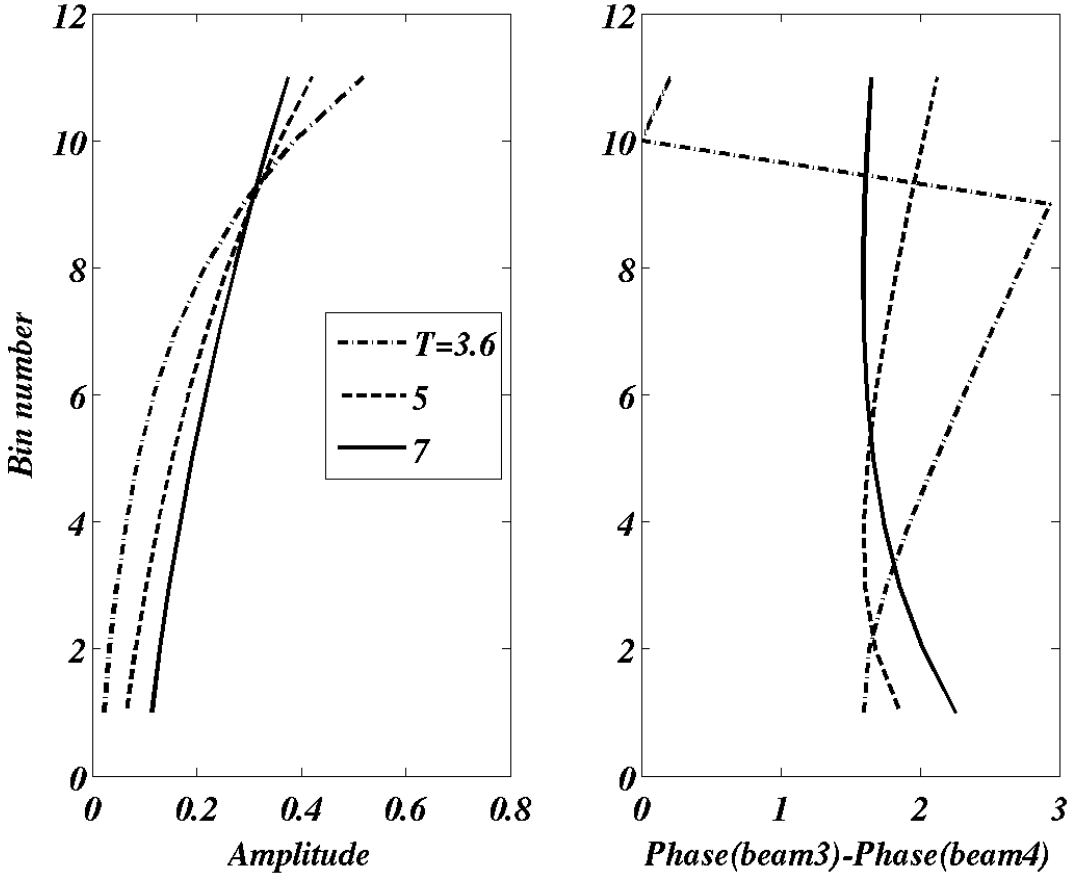

Figure 1-7. Vertical structure of the eigenvectors for three wave periods. Left: the maximum amplitude of beam velocities for beam 3 and 4. Right: phase difference between beam 3 and 4. Each curve corresponds to a different value of the wave period.

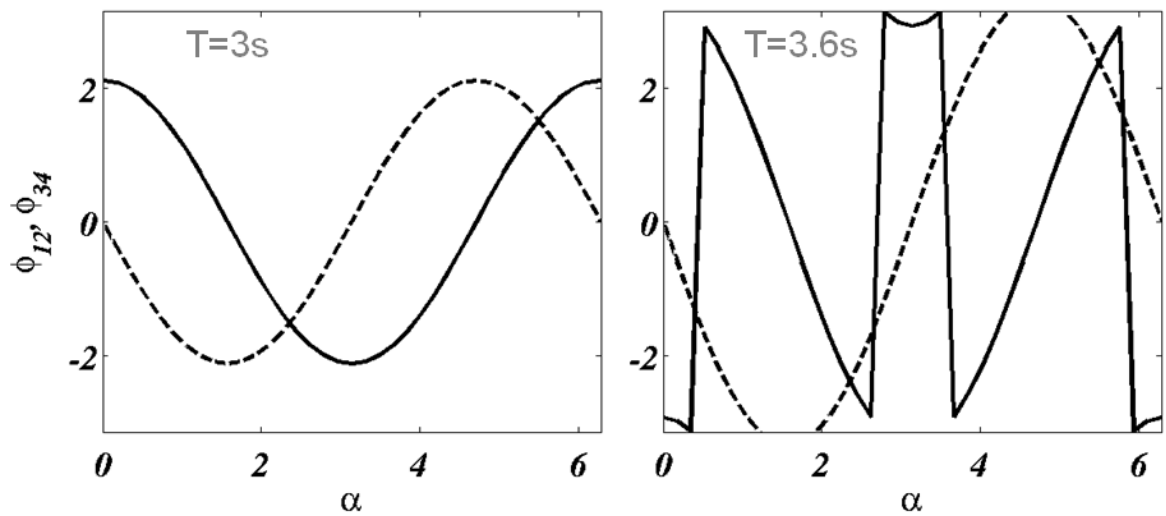

Figure 1-8. Phase differences φ_{12} and φ_{34} as a function of wave propagation angle α for two wave periods, T= 3 sec and 3.6 sec. The case illustrated on the right, the maximum phase difference exceeds 2π resulting in wrap

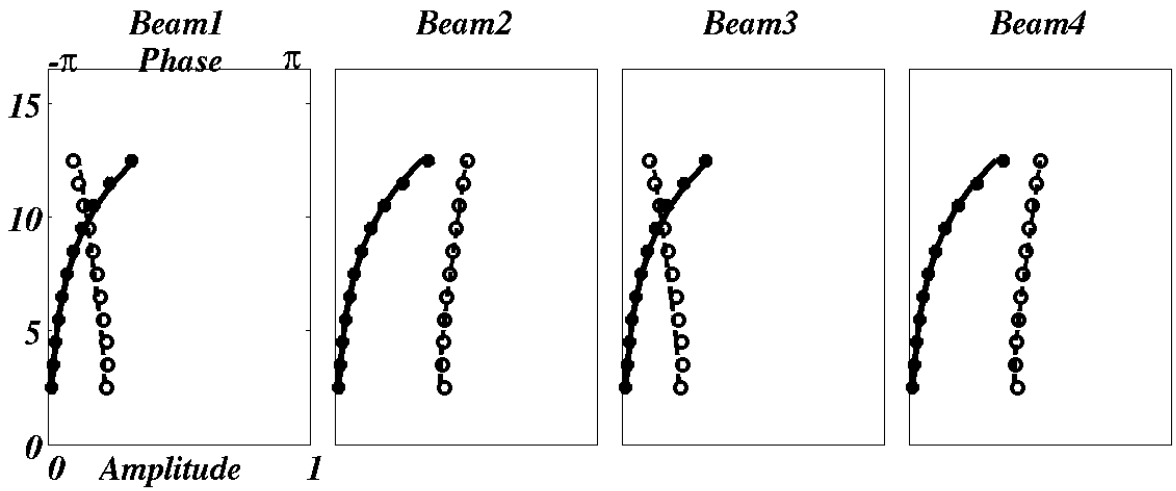

Figure 1-9. Amplitude and phase of the vertical structure of along beam velocities for beams 1-4 of ADCP West. The linear theory amplitude (solid line) and phase (dashed line) are illustrated along with the observations (solid and open circles). The complex correlation is 0.9905.

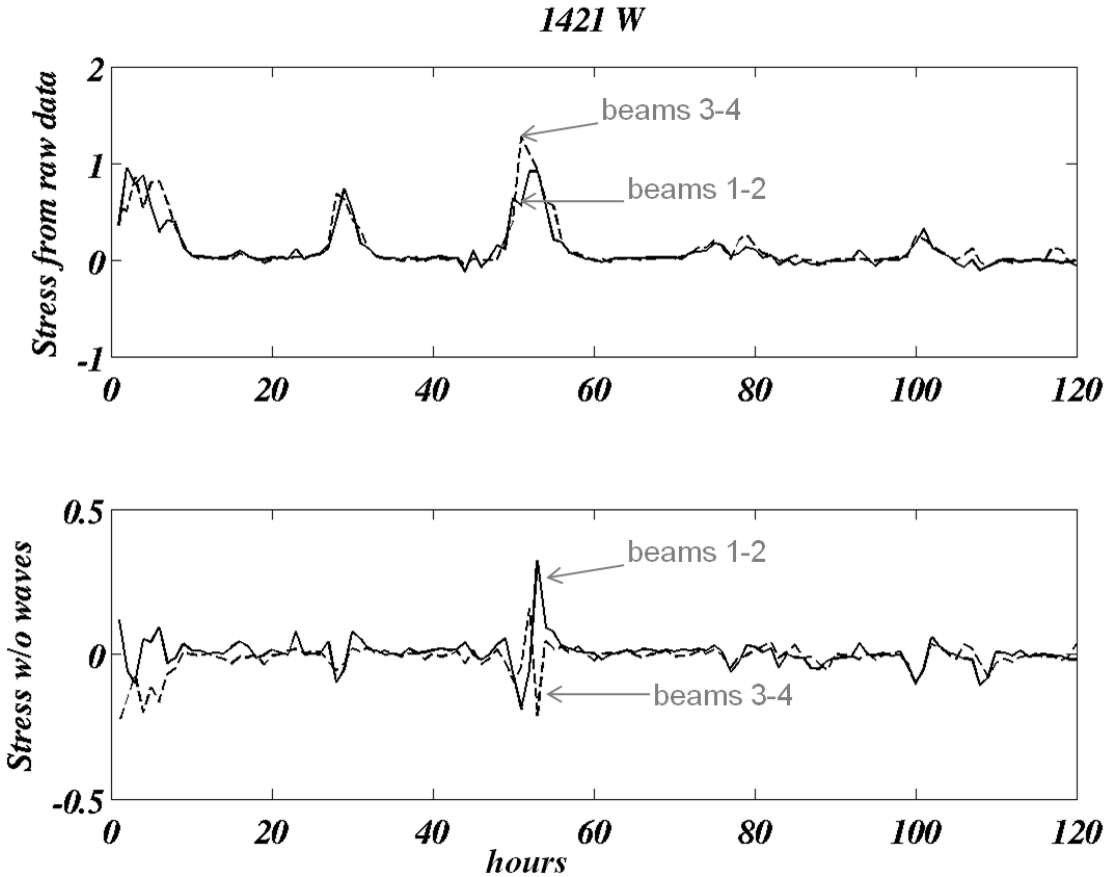

Figure 1-10. Time series of wave stresses at ADCP West estimated using the variance method (Eqn. 1-1). Top: covariance between raw beam velocities. Bottom: covariance after the wave associated beam velocities have been removed. The solid line is the Reynolds stress in the direction of beams 1-2, the dashed line is the stress in the direction of beams 3-4.

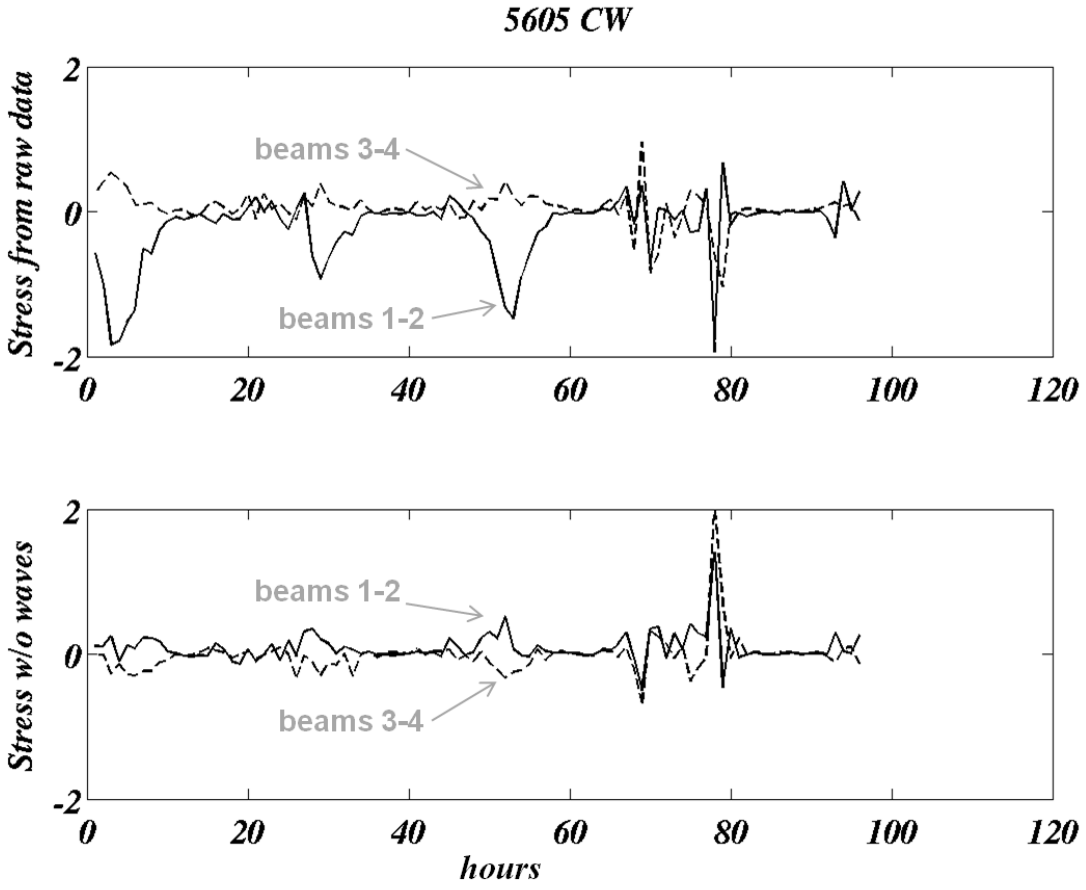

Figure 1-11. Time series of wave stresses at ADCP Center West estimated using the variance method (Eqn. 1-1). Top: covariance between raw beam velocities. Bottom: covariance after the wave associated beam velocities have been removed. The solid line is the Reynolds stress in the direction of beams 1-2, the dashed line is the stress in the direction of beams 3-4. The stress estimates before 100 hours due to instrument error.

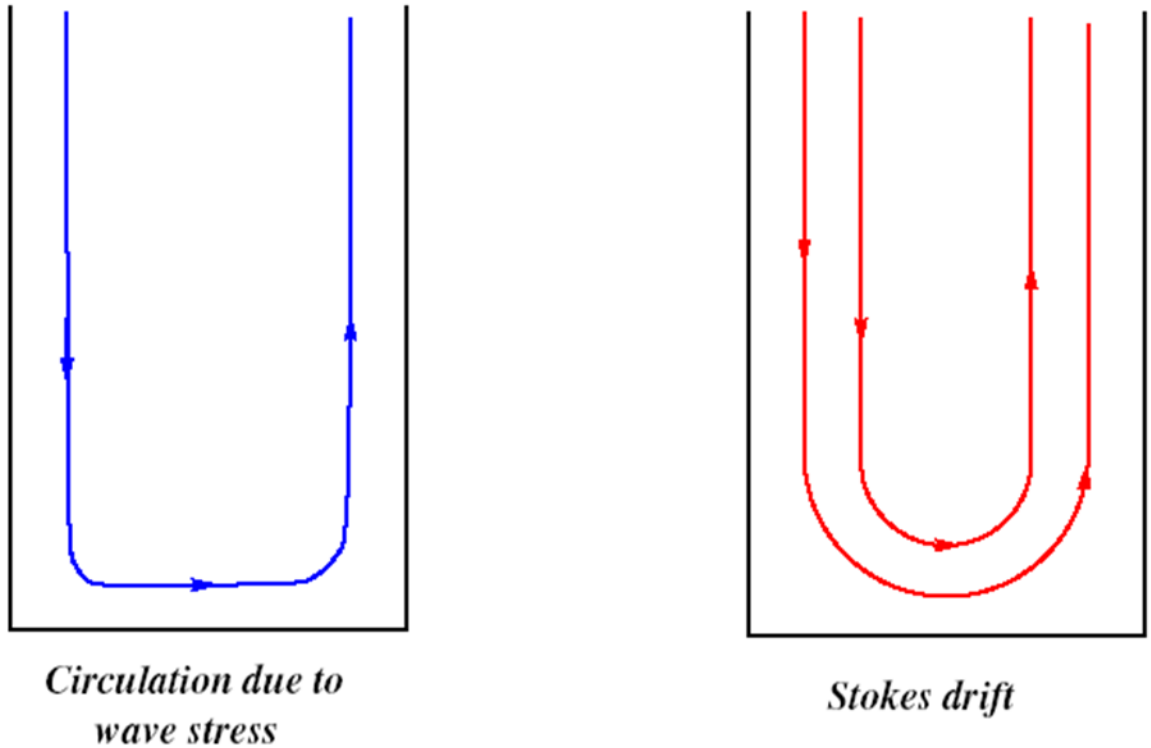

Figure 1-12. Schematics of the circulation due to wave stress and stokes drift. Left: proposed circulation corresponding to wave stress. Currents are concentrated near the edges where the waves are effected by bottom stresses (depths close to 5~6 m). Right: proposed circulation due to Stokes drift. On the right side, where the wave amplitudes are largest, the Stokes drift must be downwave or toward the closed end. On the left side, the wave amplitude is small therefore the stokes drift itself would be close to zero. Mass conservation requires the downwave flow to return toward the ocean and it seems reasonable that this return flow would be on the left side.

CHAPTER 2
STRATIFIED WIND-DRIVEN FLOWS

Introduction

Numerical and analytical models of wind-driven flow in a constant density, semienclosed basin with lateral variations in bathymetry predict downwind flow over shallow areas and upwind flow in the deepest part of the cross-section (Csanady 1973; Mathieu et al. 2002; Winant 2004; Sanay and Valle-Levinson 2005). Observations in a Gulf of California bay during practically unstratified conditions showed, however, a different structure. Downwind flow appeared to occupy the entire water column on the right, relative to the wind direction, and upwind flow developed over the left portion of the cross-section. Differences between theoretical results and observations were attributed mainly to three factors (Ponte et al. 2011): a) influence of advective accelerations; b) effects of lateral shear in wind stress (wind stress curl); and c) lack of a well-defined channel flanked by distinct shoals. The analysis presented in Chapter 1 suggests that wave stresses might also be responsible for the discrepancy. Advective accelerations and wind stress curl have not been considered in previous analytical solutions and both seem to favor the wind-driven flow structure observed during the unstratified season. However, the results of Sanay and Valle-Levinson (2005) did include effects of advective accelerations and still showed the response of downwind flow over shoals and upwind flow in the channel. It has been shown that this pattern can be modified by the shape of the bathymetry (Valle-Levinson 2011). However, little is known about the response of stratified flows to wind forcing in a semienclosed system. The purpose of this study is to explore with observations the subinertial flow patterns in a stratified bay of the Gulf of California, Bahia Concepcion. This bay is

located near an amphidromic point for semidiurnal tides, thus minimizing the effects of semidiurnal tidal forcing and allowing determination of stratified flow structures caused by other forcings, such as wind.

Observations

Observations of current velocity profiles and discrete temperature time series were obtained in a semienclosed bay, Bahía Concepción, in the Gulf of California (Figure 1-1). Measurements were recorded during the strongest water column stratification of the year (Cheng et al. 2010), from July to October 2005. The bay is 40 km long, 5 to 10 km wide. The northern half of the bay has a southeastward orientation that changes to southwestward in the middle of the bay. The southern half of the bay also displays a southeastward orientation and the bathymetry resembles a bowl shape with greatest depths reaching 30 m slightly biased toward the west. The bathymetry of the transect sampled (Figure 1-1) featured an asymmetric U shaped distribution with maximum depth of 30 m shifted to the left (looking seaward) from the middle.

Measurements were collected in the southern half of the bay, where the bathymetry is least complicated. Velocity profiles were obtained with 7 bottom-mounted RD Instruments ADCPs recording every 10 minutes and distributed along a cross-bay transect ~6 km long. The main driving forces in the bay during the period of observation were the wind and the diurnal tides. Winds were predominantly from the south, with well-defined diurnal (sea-breeze) and synoptic (2-7 days) temporal variability.

Diurnal astronomic tides contributed to enhance diurnal seabreeze effects. In this study, however, the high frequency (periods < 40 h) variability is filtered out with a Lanczos filter to study subinertial variations of exchange flows under stratified conditions. Moreover, in order to synthesize nearly 3 months of velocity profiles at 7

locations, an Empirical Orthogonal Functions (EOFs) analysis is carried out with the records. This analysis identifies the dominant structure of flow profiles at all stations, simultaneously, and describes the temporal variability of all profiles. Because this is a statistical approach to separate a set of time series in different modes of variability, it is sometimes challenging to find a physical connection between the statistical EOF modes and a causative effect. In this study, at least the most relevant mode is related to a causative effect as presented in the results.

Results

Time series of temperature profiles in the middle of the transect show the water column to be stratified with typical surface-to-bottom differences of 10ºC in 20 m depth (Fig. 2-1a). Heat content clearly increases throughout the water column from the beginning to the end of the deployment. Most of the heat content change has been attributed to atmospheric heat fluxes, although the largest changes during the first month are caused by advective transport of upwelled waters from outside the bay mouth (Cheng et al. 2010). Maximum water column stratification is close to 4 ºC/m in the middle of the deployment (days 234-235, Figure. 2-1b), coinciding with a surface increase and bottom decrease in temperature. The thermocline, which likely coincides with the pycnocline and is represented by the darkest blue shades in Figure 2-1b, migrated vertically from a depth of ~10 m at the beginning of the deployment in July to a depth close to 20 m after day 235 (August 23rd). The thermocline deepening is associated with atmospheric heating between July and September. Anomalies in stratification strength are calculated as the difference between the time series of maximum stratification in the water column and a 10-day running mean of the same signal. Oscillations of this anomaly, which can be regarded as oscillations of the

thermocline, are shown in Figure 2-1c and display a maximum spectral peak (not shown) at a period of ~13 days associated with the beating of the two tidal diurnal constituents, or the interaction between the diurnal sea breeze and the diurnal tide (O_1). Pycnocline oscillations also showed prominent spectral peaks at periods of 5 days related to wind forcing.

Low-pass filtered flows show more complicated structures than expected from theory. The western half of the cross-section, displays flows going in one direction while at the other side, water flowed in the opposite direction (e.g. day 278, Figure 2-2). Also, flows appear vertically sheared over some of the stations but they are vertically uniform or sheared in the opposite direction in other stations (e.g. day 195 or 210). These flows show no clear or obvious relationship to wind forcing.

In order to investigate the different modes of variability of subinertial flows, they are decomposed in empirical orthogonal functions (EOFs). Mean flows (Figure 2-3) are first subtracted before applying the EOFs. Mean flows show a depth-dependent recirculating structure with the flow over the western half of the transect (left on Figure 2-3) moving into the bay at maximum mean speeds of 3.5 cm/s centered at 13 m depth. Flow in the opposite direction develops in the eastern half (right half looking seaward), occupying a greater area of the cross-section than the inflowing portion but with weaker speeds of <2 cm/s and centered at ~18 m. Lateral flows depict eastward (from left to right) motions associated with the mean cyclonic recirculation. Near the surface, the flow moves seaward with the deployment-mean wind. The structure of mean flows during this stratified season is comparable, at least below 8-10 m depth, to that observed during a period of unstratified conditions (Ponte et al. 2011). The distinct

difference between unstratified and stratified water column is the downwind flowing upper-most part of the water column (above 10 m).

The cyclonic recirculation observed throughout the water column during unstratified conditions is attributed to advective accelerations and lateral shears of wind stress (Ponte et al. 2011) and to wave stresses (Winant, 2011). Persistence of such recirculation during stratified conditions, albeit below a surface layer ~8 m thick, suggests that advective accelerations caused by diurnal (tidal or sea breeze forcing) forcing are likely most influential in the recirculation development. Deviations from the mean flow structure during stratified conditions are described by the spatial and temporal structures of the EOFs.

Analysis of empirical orthogonal functions of the principal-axis flow component at each site indicates that the first 6 modes explained 80% of the flow variability. The first two modes explain 27 and 17% of the variability, respectively (Figure 2-4). Therefore, there is no predominantly energetic mode of variability. All of the modes exhibit a rich spatial structure with vertical and lateral variations (Figure 2-4). Mode 1 shows a vertically varying structure with negative values at the surface, indicating seaward flows whenever the coefficients shown in Figure 2-5 were positive. Positive values of the temporally varying coefficients (Figure 2-5) are associated with upward water level slopes from head to mouth of the bay and northward winds (Figure 2-2).

The strongest flows associated with Mode 1 appear on the western portion of the bay, where the flow is essentially two-layered: downwind at the surface and return flow underneath. Appearance of the strongest flows on the western portion of the bay could be related to the coastal morphology and bathymetry that causes wind and flow

acceleration around the curving coastline and bathymetry (see Figure 1-1). Interestingly, the spatial structure of Mode 1 is also laterally sheared at the surface, within the uppermost 10 m. Recirculation above the pycnocline is likely associated with this distribution.

Another interesting feature of the spatial structure of Mode 1 is the near-bottom negative portion over the eastern side of the bay. It is possible that this flow is caused by hypersaline and inverse longitudinal density gradient conditions in the bay, driving near-bottom outflow. Obviously, this could only happen during the times of positive values of the temporally varying coefficients (Figure 2-5). Density-driven flows should have magnitudes of (Officer 1976) $g\ G\ H^3/(48\ \rho\ A_z)$, where g is gravity's acceleration, G is a horizontal density gradient, H is water column depth, ρ is a reference water density, and A_z is a vertical eddy viscosity. For H of 25 m in Bahia Concepcion, taking A_z of 1×10^{-4} to1×10^{-3} m^2/s, would require a G of between 1×10^{-6} kg/m^4 and $\times10^{-5}$ kg/m^4 for a density-driven flow of ~0.05 m/s. Values of G on this order of magnitude were observed in the bay during that time of year (Cheng et al. 2010) and therefore it is possible that density-driven flows could have complicated the picture a bit more.

Mode 1 has a clear correspondence to water level slope (Figure 2-5) and shows, through the spectrum of its time-varying coefficients, dominant periods of variability associated to monthly oscillations (0.03 cpd), long-term modulation of diurnal forcing (0.07 cpd) and synoptic-scale forcing (0.2 cpd).

Mode 2 shows a laterally sheared structure (Figure 2-4) that indicates a cyclonic recirculation when the coefficients of Mode 2 are negative (Figure 2-5). Flow structures observed during periods of negative Mode 2 coefficients are consistent with the cyclonic

gyre structure observed in the unstratified season (Ponte et al. 2011). Mode 2 is related to the cross-sectional mean flow, an indication of remote forcing from the Gulf of California. It is possible then that remote forcing causes laterally sheared flows. The spectral energy of Mode 2 coefficients showed synoptic-scale variability and long-term (period >1 month) variability that was probably related to a trend for Mode 2 to become more positive, thus generating a recirculation in the opposite sense: seaward over the left and landward over the right portion of the cross-section (looking seaward).

For all modes there is vertically sheared bidirectional flow, as expected from theory, with the largest amplitude asymmetrically influenced by Earth's rotation for modes 3, 4 and 6. Some of the modes show three-layered responses in the deepest part of the section. In addition to wind, density-driven flows could influence the appearance of the third layer, as suggested from scaling of the baroclinic pressure gradient.

Conclusions

Analysis of current velocity profiles measured at a cross-section in a semiarid bay of the Gulf of California during the stratified season reveal complex flow structures. A cyclonic recirculation observed during unstratified conditions persists below the thermocline during the stratified season. Such recirculation is thought to be caused by a relatively flat bathymetry and the influence of advective accelerations. Above the thermocline, the flow moves downwind. Within the rich spectrum of variability in the flow structure observed, the dominant mode is vertically sheared for the most part of the cross-section and explains only ~27% of the variability observed. This mode of variation is related to water level slopes driven by wind forcing and exhibit an interesting modulation (~13 days) likely caused by the interaction between sea breeze and diurnal (O1) tide.

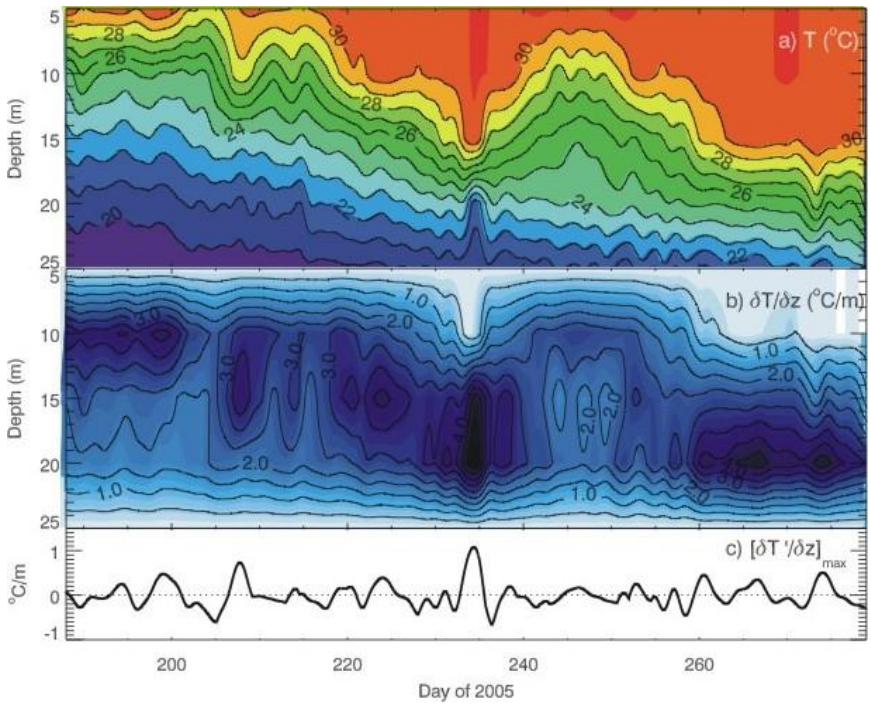

Figure 2-1. Records from thermistors deployed every 5 m depth in the middle of the sampling cross-section. a) Time series of temperature profiles with a contour interval of 1ºC. b) Vertical gradient of temperature (absolute value contoured at intervals of 0.5ºC/m). c) Deviations from a 10-day running mean of the maximum temperature gradient.

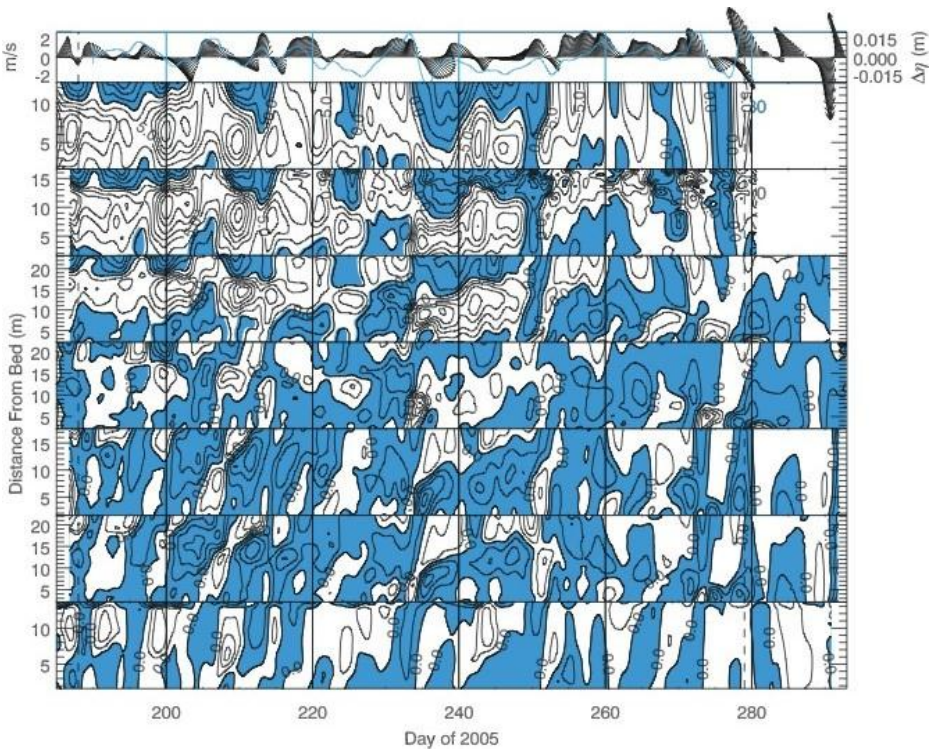

Figure 2-2. Time series of wind velocity (showing direction toward which the wind blows) and low-pass filtered water level difference between mouth and head of the bay (upper panel). Positive values denote higher elevation at the mouth. Subsequent panels show low-pass filtered profiles of principal-axis component of flow at each one of the seven moorings. Negative values (shaded in blue) indicate seaward flow. Contour interval is 2.5 cm/s

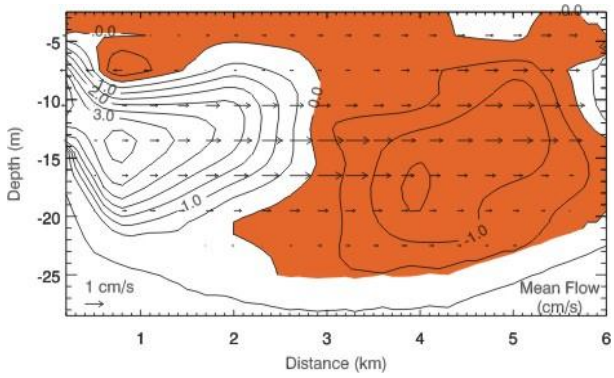

Figure 2-3. Mean flows (cm/s) throughout entire deployment, looking seaward. Orange-shaded contours indicate seaward flows. Arrows denote cross-bay flows

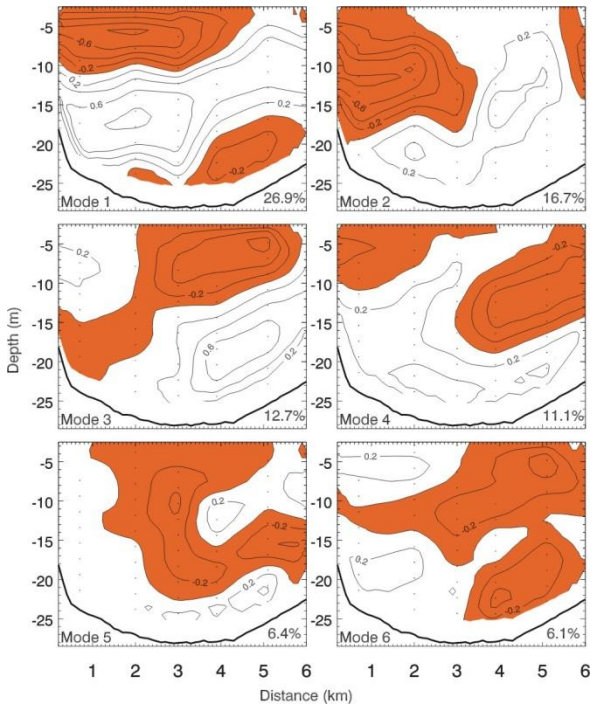

Figure 2-4. Spatial structure of EOF modes. Looking seaward. Orange contours indicate seaward motion when the coefficients of Figure 6 are positive.

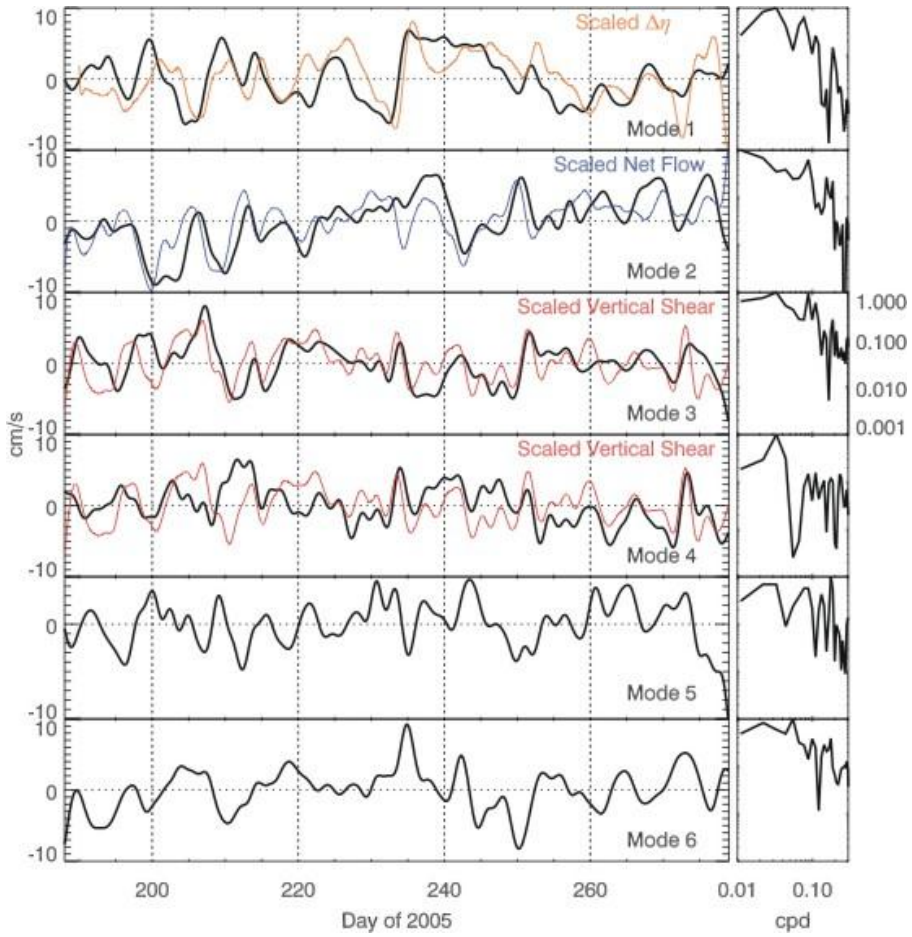

Figure 2-5. Time series of each EOF coefficient and spectra illustrating the variability of each time series. The upper 4 panels also show scaled versions of possible forcing agents with signs inverted.

LIST OF REFERENCES

Caliskan, H. and A. Valle-Levinson, 2008. Wind-wave transformations in an elongated bay, *Cont. Shelf Res.,* **28**, 1702-1710.

Cheng, P., A. Valle-Levinson, C. D. Winant, A. Ponte, G. Gutierrez de Velasco and K. Winters, 2010. Upwelling-enhanced seasonal stratification in a semiarid bay. *Cont. Shelf Res.*, **30**, 1241-1249.

Csanady, G. T., 1973: Wind-induced barotropic motions in long lakes.*J. Phys. Oceanogr.,* **3,** 429–438.

Dean, R. G. and R. A. Dalrymple, 1991: *Water wave mechanics for engineers and scientists*. World Scientific Publishing, Singapore, 353 pp.

Emery, W. J. and R. E. Thomson, 2001: *Data analysis methods in physical oceanography.* Elsevier, Amsterdam, 2nd edition.

Feddersen, F., R.T. Guza, S. Elgar, and T.H.C. Herbers, 1998: Alongshore momentum balances in the nearshore, *J. Geophys. Res*., **103**, 15667-15676.

Fewings, M., S. J. Lentz, and J. Fredericks, 2008: Observations of cross-shelf flow driven by cross-shelf winds on the inner continental shelf. *J. Phys. Oceanogr*., **38**, 2358–2378.

Hendershott, M. C. and A. Speranza, 1971: Co-oscillating tides in long, narrow bays; the Taylor problem revisited. *Deep Sea Research*, **18**, 959–980.

Johnson, M. and J. Ledesma-Vásquez, 2001: Pliocene-Pleistocene rocky shorelines trace coastal development of Bahía Concepcíon, gulf coast of Baja California Sur (Mexico). *Palaeogeogr., Palaeoclimateol., Palaeoecol*., **166**, 65–88.

Kirincich, A.R., S.J. Lentz, and G.P. Gerbi, 2010: Calculating Reynolds stresses from ADCP measurements in the presence of surface gravity waves using the cospectra fit method. *J. Atmos. Oceanic Technol*., **27**, 889–907

Li, C., and J. O'Donnell, 2005: The effect of channel length on the residual circulation in tidally dominated channels. *J. Phys. Oceanogr.,* **35,** 1826–1840.

Lohrmann, A., B. Hackett, and L. P. Roed, 1990: High resolution measurements of turbulence, velocity, and stress using a pulse-to-pulse coherent sonar. *J. Atmos. Oceanic Technol.*, **7**, 19–37.

Longuet-Higgins, M. S., 1970: Longshore currents generated by obliquely incident sea waves 1, *J. Geophys. Res*., **75**, 6790– 6801.

Lu, Y. and R. G. Lueck, 1999: Using a broadband adcp in a tidal channel. Part ii: turbulence. *J. Atmos. Oceanic Technol*., **16**, 1568–1579.

Mathieu, P. P., E. Deleersnijder, B. Cushman-Roisin, J. M. Beckers, and K. Bolding, 2002. The role of topography in small wellmixed bays, with application to the lagoon of Mururoa. *Cont. Shelf Res.,* **22,** 1379–1395.

McFall, C., 1968: Reconnaissance geology of the Concepcion bay area, Baja California, Mexico. Stanford University Publications, Geological Society, **10**, 1–25.

Morales, R. A. and G. Gutiérrez, 1989: Role of lateral gradients and longitudinal dispersion in the salt balance of a shallow, well-mixed estuary. *Geofsica Internacional ,* **28**, 25–46.

Polton, J., D. Lewis, and S. Belcher, 2005: The role of wave-induced coriolis-stokes forcing on the wind-driven mixed layer. *J. Phys. Oceanogr*., **35**, 444–457.

Officer, C.B., 1976. Physical Oceanography of Estuaries(and Associated Coastal Waters). John Wiley, New York, 465pp

Ponte, A., G. Gutiérrez De Velasco, A. Valle-Levinson, K. Winters, and C. D. Winant, 2011. Wind-driven subinertial circulation inside a semi-enclosed bay in the Gulf of California. Submitted to J. Phys. Oceanogr.

Rosman, J. H., J. L. Hench, J. R. Koseff, and S. G. Monismith, 2008: Extracting Reynolds stresses from Acoustic doppler Current Profiler measurements in wave-dominated environments. *J. Atmos. Oceanic Technol*., **35**, 286–306.

Sanay, R., Valle-Levinson, A., 2005. Wind-induced circulation in semienclosed homogeneous, rotating basins. J. Phys. Oceanogr. 35, 2520–2531.

Shaw, W. J. and J. H. Trowbridge, 2001: The direct estimation of near-bottom turbulent fluxes in the presence of energetic wave motions. *J. Atmos. Oceanic Technol.,* **18**, 1540–1557.

Stokes, G. G., 1847, On the theory of oscillatory waves, *Trans. Camb. Soc*., **8**, 441-455 (reprinted in *Mathematical and Physical Papers*, London, **1**, pp 314-326)

Trowbridge, J. H., 1998: On a technique for measurement of turbulent shear sterss in the presence of surface waves. J. Atmos. Oceanic Technol., 15, 290–298.

Valle-Levinson, A., 2011. Large Estuaries (Effects of Rotation), in Treatise on Estuarine and Coastal Science, Elsevier, in press

Whipple, A. C., R. A. Luettich, and H. E. Seim, 2006: Measurements of reynolds stress in a wind-driven lagoonal estuary. *Ocean Dyn*., **56**, 169–185.

Winant, C.D., 2004. Three dimensional wind-driven flow in an elongated, rotating basin. J. Phys. Oceanogr. 34, 46

Xu, Z. and A. J. Bowen, 1994: Wave- and wind-driven flow in water of finite depth. *J. Phys. Oceanogr.*, **24**, 1850–1866.

BIOGRAPHICAL SKETCH

Chloé Daisy Winant was raised in Solana Beach, CA, with views from her kitchen window of the Pacific Ocean and San Elijo Lagoon. She received her B.A. in geophysics from Occidental College in 2002, and worked as a research assistant for four years on various oceanographic experiments. In the early months of 2006, she met her future graduate advisor at a meeting and that fall began her PhD in coastal engineering at the University of Florida. In December 2011, Chloé was honored to receive her doctorate degree in front of friends and family.